



## Examination of the microscopic definition for granular fluidity

James A. Robinson  and Daniel J. Holland \*

*Chemical and Process Engineering Department, University of Canterbury, Christchurch 8140, New Zealand*

Luke Fullard 

*School of Fundamental Sciences, Massey University, Palmerston North 4474, New Zealand*



(Received 23 July 2020; accepted 15 February 2021; published 8 April 2021)

Recent work has used an introduced property, termed granular fluidity (defined as the shear rate divided by the stress ratio), to help quantify and model nonlocal behavior within granular flows. A so-called “microscopic” definition was subsequently proposed which links this granular fluidity to the packing fraction, particle diameter, and the granular temperature. This definition provides a physical basis on which the nature of granular fluidity can be understood. Here we have examined the microscopic definition, first replicating the previously demonstrated behavior using DEM simulations of shear cells and then demonstrating that the relationship’s coefficients are dependent on the coefficient of friction, the presence of tangential damping, and the presence of rolling resistance. When the geometry is changed from a shear cell to a cylindrical hopper, the relationship shifts away from the expected response, thus demonstrating that there are geometry dependent effects that are not captured by the original formulation. This shows that granular fluidity is more complex than previously thought and that the current microscopic definition is insufficient.

DOI: [10.1103/PhysRevFluids.6.044302](https://doi.org/10.1103/PhysRevFluids.6.044302)

### I. INTRODUCTION

While granular flows are ubiquitous in both nature and industry, modeling such flows continues to present significant challenges. One such challenge is that stress at a point within a granular medium does not solely depend on the local properties, such as the shear rate, but also on behavior in neighboring regions. It is thus “nonlocal” and difficult to describe as a continuum. The development of models that can account for the nonlocality of granular flow is essential to predict large-scale, complex granular systems using a continuum description [1]. One such model is the nonlocal granular fluidity model [2,3]. The model introduces a property, termed granular fluidity, which is defined based on the local stress and shear rate. The transport of granular fluidity is described by a partial differential equation (PDE) that must be solved in order to model a system. While far from the only nonlocal model developed [1], this model is of interest due to a recent attempt that was made to develop a definition for the model’s version of granular fluidity based on measurable state parameters of the flow, a so-called “microscopic definition” [4]. Here we investigate this microscopic definition of granular fluidity further to test the limits of its validity for more complex flow conditions.

The granular fluidity model is related to the earlier  $\mu(I)$  rheology [5,6], which is widely used to describe granular flow. The  $\mu(I)$  rheology relates the inertial number to  $\mu$ , the ratio of shear stress and pressure. The inertial number  $I$  is considered as the ratio of an inertial timescale (defined as

---

\*Corresponding author: [daniel.holland@canterbury.ac.nz](mailto:daniel.holland@canterbury.ac.nz)

the square root of the particle density divided by the pressure, multiplied by the particle diameter) and a shear dependent timescale (defined as the inverse of the shear rate). The relationship between  $I$  and the  $\mu$  is then typically described using fitted (empirical) equations. The  $\mu(I)$  rheology is a local rheology, and so stress is a function of the local shear rate and pressure only and is not directly influenced by nearby flow features. The  $\mu(I)$  rheology has been successful at capturing the behavior of simple granular systems, such as flow down a pile [6], column collapse [7], or hopper flows [8]. However, because it is a local model it cannot capture nonlocal effects, such as creeping flow in regions where  $\mu$  is less than the static yield value,  $\mu_s$  [9–11], or jamming in regions where local rheology predicts flow [12]. The inability of local rheology to capture these effects necessitates the use of a nonlocal rheology. Kinetic theory is one such nonlocal rheology, which has been well validated for dilute granular flows [13] but is not readily applicable to dense granular flows [14]. The nonlocal granular fluidity model [3] and the gradient model [1] are both examples of newer models developed for dense granular flows. These models have been shown to be capable of capturing nonlocal effects that cannot be described by the  $\mu(I)$  rheology [15], demonstrating the advantages of these new models over the older rheology.

The nonlocal rheology model developed by Kamrin and Koval [2] defines granular fluidity ( $g$ ) as

$$g = \frac{|\dot{\gamma}|}{\mu}. \quad (1)$$

In Eq. (1)  $|\dot{\gamma}|$  is the equivalent shear rate, and  $\mu$  is the bulk granular friction defined as the ratio of the equivalent shear stress ( $|\sigma|$ ) to the pressure ( $P$ ) (see Appendix A 2 for full definitions of these properties). In the continuum model, the granular fluidity is described by a PDE that characterizes the transportation, generation, and dissipation of the fluidity throughout the system. The model has successfully captured a variety of nonlocal flow features in systems such as annular flow [2,3] and inclined plane flow [16,17].

One significant issue with the concept of granular fluidity is that its physical meaning is unclear. Additionally, Bouzid *et al.* [1] noted that the granular fluidity, as originally defined, is not a state variable, which is necessary for its use in continuum modeling. Recently, in order to provide a physical basis for granular fluidity by linking it to state variables, Zhang and Kamrin [4] proposed the following relationship to define fluidity:

$$\frac{gd}{\delta v} = F(\phi). \quad (2)$$

Here  $d$  is the local average particle diameter and  $\delta v$  is the square root of the local granular temperature, which is a measure of the fluctuations in particle velocity (see Appendix A 2 for a full definition of  $\delta v$  as well as the average diameter).

The definition in Eq. (2) links granular fluidity to the velocity fluctuations and defines the resulting dimensionless number, termed here as the dimensionless granular fluidity (or  $gd/\delta v$ ), as solely a function of the packing fraction ( $\phi$ ). To examine this relationship Zhang and Kamrin [4] ran multiple discrete element method (DEM) simulations of shear cells (varying the gravity, the top surface velocity, and the confining pressure) and chute flows (varying the inclination angle and either the confining pressure or the volume). The results of these simulations all collapsed onto a single curve when  $gd/\delta v$  was plotted against  $\phi$ , providing a justification for their chosen definition. They defined the empirical relationship

$$F(\phi) = 2 - \frac{(\phi - 0.58) + \sqrt{(\phi - 0.58)^2 + 1.54 \times 10^{-4}}}{0.048}, \quad (3)$$

to describe the collapse that they observed. Later works examining shear cell simulations recovered a similar dependence on the solid fraction [18,19], though did not attempt to confirm that Eq. (3) is recovered. An analysis of 2D hopper flow also produced a similar functional relationship [20], though it was not quantitatively similar due to the different packing fractions possible in 2D flow.

Other models have been developed which capture nonlocal behavior with varying degrees of success. Aside from the gradient model and kinetic theory, other models include partial fluidization theory [21] and the eddy viscosity model [22]. These models, and others, have been reviewed comprehensively [1,23]. These models each suggest their own mechanisms underlying nonlocality. Recent work shows that additional parameters, such as force chain fluctuations [24], may also be relevant. The nonlocal granular fluidity model is well established for dense granular flows, having been proved capable of handling various different geometries. The addition of the microscopic definition allows a clear linking between the overarching model and the underlying mechanism of the nonlocal response. Thus, in this work focus is restricted to the nonlocal granular fluidity model and the microscopic definition of granular fluidity.

The aim of this work is to examine the microscopic definition of granular fluidity in depth to determine how it behaves under different conditions and whether it can be extended beyond the simple systems originally examined. If a consistent collapse can be demonstrated, it would provide evidence for the universality of the definition. This would reinforce its validity as a physical description of granular fluidity. DEM simulations were first run in a shear cell geometry, to replicate the prior results [4]. Additional shear cell simulations were then run with a variety of simulation parameters, including changing the interparticle friction. Finally, DEM simulations were run for a number of different hopper configurations. From these simulations  $gd/\delta v$  and  $\phi$  have been extracted to allow for comparison with Eq. (3).

## II. METHODS

The DEM simulations used to produce the data discussed in this paper were run using the open source DEM software LIGGGHTS [25]. Simulations were run using a soft sphere, Hookean contact model. The forces involved in a collision between two particles ( $\alpha$  and  $\beta$ ) are modeled as

$$\mathbf{F}_{\alpha\beta} = (K_n\delta\mathbf{n}_{\alpha\beta} - \gamma_n\mathbf{v}_{n,\alpha\beta}) + (K_t\delta\mathbf{t}_{\alpha\beta} - \gamma_t\mathbf{v}_{t,\alpha\beta}), \quad (4)$$

where the first bracketed term accounts for the normal force (between the two particle centers), while the second accounts for the tangential force (perpendicular to the normal force). The tangential force ( $\mathbf{F}_t$ ) is truncated such that  $\mathbf{F}_t \leq \mathbf{F}_n\mu_p$  (where  $\mu_p$  is the interparticle friction coefficient and  $\mathbf{F}_n$  is the normal force).  $\delta\mathbf{n}_{\alpha\beta}$  and  $\delta\mathbf{t}_{\alpha\beta}$  are the normal and tangential overlap, respectively,  $\mathbf{v}_{n,\alpha\beta}$  and  $\mathbf{v}_{t,\alpha\beta}$  are the relative normal and tangential particle velocities,  $\gamma_n$  and  $\gamma_t$  the normal and tangential damping coefficients, and  $K_n$  and  $K_t$  the normal and tangential spring constants. The torque generated on particle  $\alpha$  during a collision was described by  $\mathbf{T} = \mathbf{r}_{\alpha,c} \times \mathbf{F}_t + \mathbf{T}_{rf}$ , where  $\mathbf{T}_{rf}$  is an additional torque contribution due to rolling friction, typically set to 0 unless otherwise stated, and  $\mathbf{r}_{\alpha,c}$  is the vector running from the center of  $\alpha$  to the point of contact. The contact force and subsequently the torque were used to solve the equations of motion for each particle. Further details on the underlying equations, and how the coefficients in Eq. (4) were defined based on particle properties are detailed in the LIGGGHTS documentation [26] and more briefly in Appendix A 1.

The shear cell simulations were run using the properties outlined in Table I. These properties were set to match those used by Zhang and Kamrin [4]. In the case of the Young's modulus, Poisson's ratio and characteristic velocity, which in our implementation act as scaling coefficients to the spring constant  $K_n$ , these values were not explicitly stated so they were instead chosen to ensure that  $K_n$  meets a stiffness criteria necessary to ensure rigid particles [4], that is

$$\frac{K_n}{Pd} > 10^4. \quad (5)$$

Finally, the tangential spring constant was set as  $2K_n/7$ . For the hopper simulations identical properties were used, except that the mean particle diameter was increased to 1.2 mm to align with ongoing experimental work.

In all simulations a particle size distribution was used to prevent crystallization. A polydispersity of  $\pm 20\%$  is widely used in the literature [2,4,8,11,27,28]; however, the definition of this size

TABLE I. List of particle properties used in the base shear cell DEM simulation.

Coefficient of restitution	$e_r$	0.1
Tangential damping coefficient	$\gamma_t$	0
Coefficient of friction	$\mu_p$	0.4
Particle density	$\rho$	$2500 \text{ kg m}^{-3}$
Mean particle diameter	$d$	0.8 mm
Young's modulus	$E$	$1 \times 10^9 \text{ Pa}$
Poisson's ratio	$\nu$	0.5
Characteristic velocity	$u_c$	$1 \text{ m s}^{-1}$

distribution is not made explicit. Previously it has been shown that a uniform size distribution greater than  $\pm 15\%$  of the particle diameter is sufficient to prevent crystallization [29]. Other works utilizing DEM simulations have also implemented uniform size distributions about a mean particle diameter [30–32]. Based on these works a uniform particle size distribution ranging from 0.8–1.2 times the mean particle diameter was implemented for all simulations. It was assumed that this aligned with the definition of  $\pm 20\%$  polydispersity used in prior works. LIGGGHTS cannot directly generate a uniform particle size distribution. Instead, the distribution was approximated by using 100 discrete particle diameters linearly spaced between 0.8 and 1.2 times the mean particle diameter.

The simulations were run with a time step ( $\delta t$ ) of approximately  $0.2\sqrt{m/K_n}$  (see Appendix A 3 for exact values). This falls below the critical time step (above which instabilities propagate) defined by Tsuji et al. [33] ( $\delta t_{crit} = 0.63\sqrt{m/K_n}$ ) which is sufficient for mildly polydisperse systems with low coordination numbers [34]. Additional simulations (not shown), were run at reduced time steps to confirm minimal variation occurred.

The properties outlined so far represent the default settings used unless otherwise stated. As noted in later sections, a number of simulations were run varying one or more of these properties to examine how they would affect the results obtained.

The geometries we examined were 3D shear cells and hoppers. The basic shear cell geometry is shown in Fig. 1(a). The shear cell was filled with 7400 particles. The pressure applied to top of the cell ( $P_w$ , defined as  $4 \times 10^{-6} P_f K_n / d$ ) and the velocity of the top layer ( $V_w$ , defined as  $0.01 V_f \sqrt{K_n / d \rho}$ ) were fixed for each simulation. The shear cell was periodic along the  $x$  and  $y$  axis with the top and bottom walls made of densely packed particles with a diameter of 0.8 mm and identical properties to the bulk particles. For the shear cells, the gravitational acceleration along the  $z$  axis ( $G$ , defined as  $4 \times 10^{-7} G_f K_n d / m$ ) was typically implemented with  $G_f = 1$ , although shear cell simulations were also run without gravity ( $G_f = 0$ ). The hopper geometry evaluated is

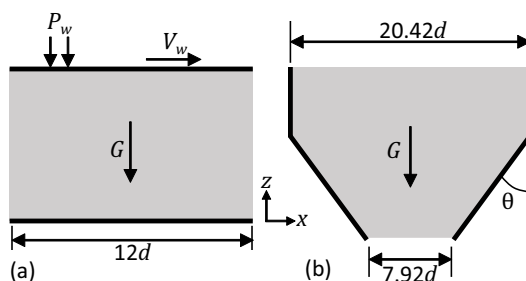


FIG. 1. Two-dimensional representations of the 3D geometries being simulated showing the  $x$  and  $z$  axes. The  $y$  axis is not shown. Panel (a) is a simple shear cell, and (b) is a cylindrical hopper. These figures are not to scale. The shear cell's width equaled its length. The height of the shear cell is not given as this was adjusted to maintain  $P_w$ . However, the height was typically around  $50d$ .

shown in Fig. 1(b). It was filled with 63 750 particles to a height of roughly  $167d$ . Three different hopper geometries were simulated using  $\theta$  values of  $90^\circ$ ,  $60^\circ$ , and  $30^\circ$ , respectively. The hopper was cylindrically symmetric and was periodic along the  $z$  axis, such that particles a short distance below the outlet of the hopper were returned to above the top surface. The hopper had smooth, frictional walls with otherwise identical properties to the particles. The hopper simulations had gravitational acceleration set with  $G_f = 1.5$ .

In order to extract bulk flow properties from the simulations, coarse graining was used. Prior works cover coarse graining in depth [35–37], so only a brief description of our implementation is included here. Packing fraction ( $\phi$ ) was defined as

$$\phi = \sum_{\alpha} V_{\alpha} W(\mathbf{x} - \mathbf{x}_{\alpha}), \quad (6)$$

and coarse-grained velocity ( $\mathbf{u}$ ) as

$$\mathbf{u} = \frac{\sum_{\alpha} V_{\alpha} \mathbf{u}_{\alpha} W(\mathbf{x} - \mathbf{x}_{\alpha})}{\sum_{\alpha} V_{\alpha} W(\mathbf{x} - \mathbf{x}_{\alpha})}. \quad (7)$$

Here  $W$  is the coarse-graining weighting function and  $\mathbf{x}$  is the current position.  $\alpha$  denotes a particular particle and so  $\mathbf{u}_{\alpha}$  is the particle's velocity,  $\mathbf{x}_{\alpha}$  the particle's position, and  $V_{\alpha}$  the particle's volume. Shear rates were calculated from Eq. (7) using central differencing.

The stress consisted of a collisional stress associated with particle contacts (the first term), and a kinetic stress associated with the motion of the particles (the second term), and was calculated from

$$\sigma_{ij} = - \sum_{\alpha} \sum_{\beta, \beta \neq \alpha} F_{\alpha\beta, i} a_{\alpha\beta, j} \int_0^1 W(\mathbf{x} - \mathbf{x}_{\alpha} + s \mathbf{a}_{\alpha\beta}) ds - \sum_{\alpha} m_{\alpha} u'_{\alpha, i} u'_{\alpha, j} W(\mathbf{x} - \mathbf{x}_{\alpha}). \quad (8)$$

$\mathbf{F}_{\alpha\beta}$  are the contact forces on particle  $\alpha$  due to the collision with particle  $\beta$ ,  $m_{\alpha}$  is the mass of particle  $\alpha$ , and  $\mathbf{a}_{\alpha\beta}$  is the difference between  $\mathbf{x}_{\alpha}$  and the point of contact between the two particles ( $\mathbf{c}_{\alpha\beta}$ ).  $\mathbf{u}'_{\alpha}$  is the difference between  $\mathbf{u}_{\alpha}$  and the coarse-grained velocity at  $\mathbf{x}_{\alpha}$ . In Eq. (8)  $\mathbf{u}$  must be evaluated at the position of each particle, however using Eq. (7) for this is computationally demanding. Instead  $\mathbf{u}$  was obtained by interpolation of the coarse-grained temporally and spatially averaged velocity field.

For our coarse graining a Lucy function was used as the weighting function:

$$W(\mathbf{r}) = \frac{105}{16\pi c^3} \left[ -3 \left( \frac{|\mathbf{r}|}{c} \right)^4 + 8 \left( \frac{|\mathbf{r}|}{c} \right)^3 - 6 \left( \frac{|\mathbf{r}|}{c} \right)^2 + 1 \right] \text{ if } |\mathbf{r}| < c, \text{ else } 0, \quad (9)$$

where  $\mathbf{r}$  is a position vector and  $c$  is the cutoff. The coarse-grained properties were analyzed as a function of the cutoff length. The properties were approximately constant for cutoff lengths around  $3d$  (data not shown). Therefore, a cutoff length of  $3d$  was used in all subsequent analysis. With this cutoff length the standard deviation, or coarse-graining width ( $w$ ), was equal to  $1.5d$ , half  $c$ .

When evaluating the shear cell simulations,  $gd/\delta v$  and  $\phi$  were calculated at discrete heights. At each height the coarse-grained properties were spatially averaged over 16 points spaced across the  $xy$  plane and then these were averaged across 100 time steps spaced 100 000 DEM time steps apart. This averaging was deemed sufficient to minimise noise in the results (see Appendix A 6 for further details). When gravity was present, a cutoff was imposed where the minimum height evaluated was  $15d$  (though in a few cases where the systems were more or less agitated the cutoff was changed to  $10d$  or  $20d$ , respectively). The cutoff was necessary to remove data in the dense slow-moving region of the flow, where granular temperature and equivalent shear rate approach 0 and so large errors can occur when calculating  $gd/\delta v$ . The choice of cutoff is expanded upon in Appendix A 6. Additional

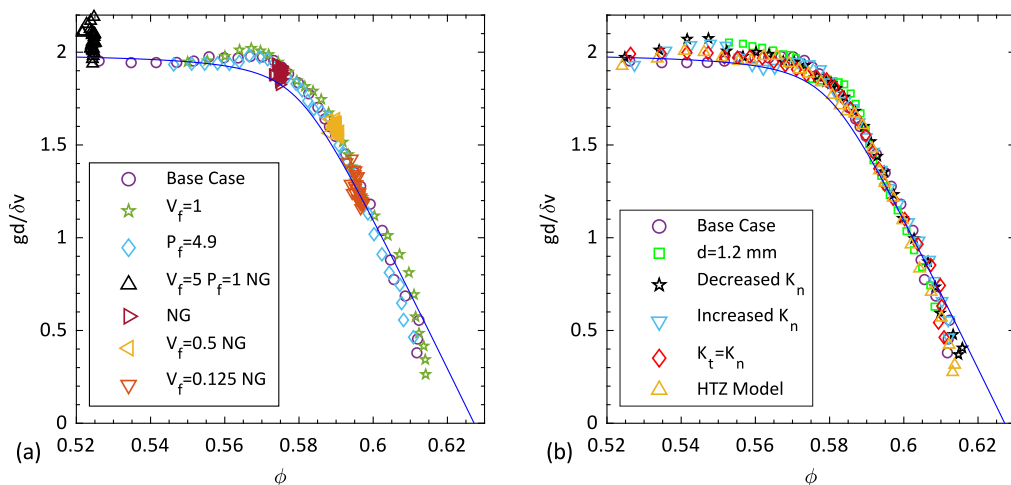


FIG. 2. Examination of  $gd/\delta v$  vs  $\phi$  for different shear cell simulations. Panel (a) has simulations where  $G_f$ ,  $V_f$  and  $P_f$  are varied from the default, and (b) has simulations where the simulation properties are altered from the default while  $G_w$ ,  $V_w$ , and  $P_w$  are kept constant. Simulations with  $G_f$  set to 0 are denoted by NG.

validation work was also carried out to confirm the expected stress profiles were recovered from the shear cell simulations (see Appendix A 6).

For the hopper simulations two different methods of analysis were considered. First,  $gd/\delta v$  and  $\phi$  were calculated at a number of radial and vertical positions near the outlet. The results were averaged spatially. In this case, for each specific radial and vertical position 10 different angles were averaged. Spatial averages were calculated in cylindrical coordinates by calculating the Cartesian components at each angle, then applying a transformation to cylindrical coordinates before averaging. Second,  $gd/\delta v$  and  $\phi$  were calculated at a series of discrete points located at different vertical positions along the centerline of the hopper. Spatial averaging was not implemented and calculations were done in Cartesian coordinates. For both methods the resulting values were averaged across 200 time steps recorded 50 000 DEM time steps apart. The number of time steps averaged across was increased compared to the shear cell simulations to compensate for the lack of spatial averaging when conducting the analysis along the centerline.

For both systems the points evaluated had the edge of the cutoff of the coarse-graining function 1.5 times the maximum particle radius from the walls to avoid any effects occurring due to particles interacting with the walls. The systems were evaluated at steady state, determined to be when the properties of interest appeared stable with time. Typical flow profiles for each system are provided in the Appendix A 4.

### III. RESULTS

#### A. Analysis of shear cell results

Figure 2(a) shows the results of simulations run with and without gravity where the values of  $V_w$  and  $P_w$  were varied, to compare with the established results [4]. The packing fraction ( $\phi$ ) has been plotted against the dimensionless granular fluidity defined by Eq. (2) (i.e.,  $gd/\delta v$ ). The curve described by Eq. (3) is also shown. The base case for the shear cell was defined as  $V_f = 3$ ,  $P_f = 3$  and  $G_f = 1$ ; variations from the base case are noted in the legend. Figure 2(a) shows that for these simulations, the dimensionless granular fluidity collapses onto a single curve for all applied pressures and velocities. At low packing fractions the curve is approximately constant. It declines

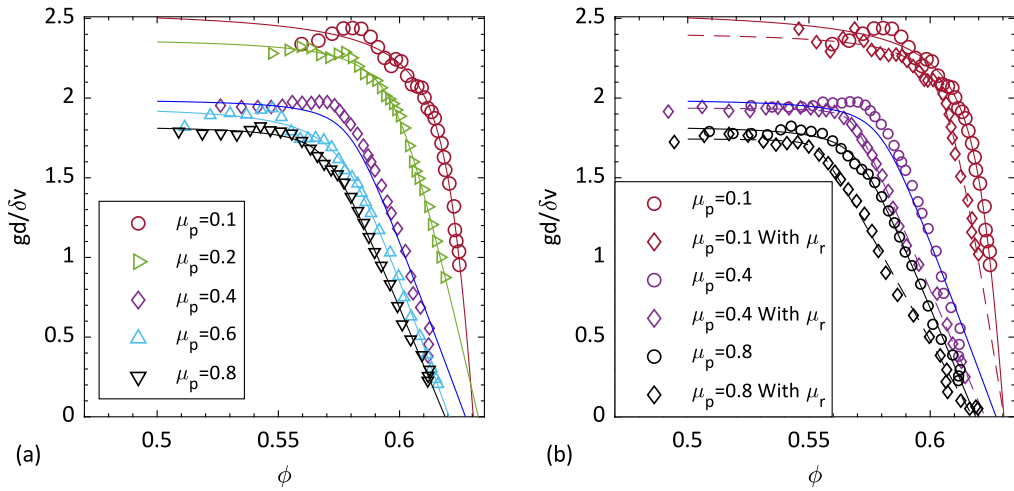


FIG. 3.  $gd/\delta v$  plotted against  $\phi$  for shear cell simulations with  $\mu$  being varied. Panel (a) shows results with solely  $\mu_p$  being varied, and (b) shows results where  $\mu_p$  is varied with or without rolling friction ( $\mu_r$ ). The lines represents the fitted Eq. (3) (fitted to all simulation except  $\mu_p = 0.4$ ). A dashed line is used for the cases with  $\mu_r$ .

steeply as it approaches higher packing fractions, the drop off beginning when  $\phi$  is around 0.58. The data obtained show good agreement with Eq. (3), confirming the expected result is recovered [4].

To further test the generality of the model, simulations were run varying a number of parameters, while keeping  $V_w$ ,  $P_w$ , and  $G$  as defined in the base case. Starting from the same base simulation as in Fig. 2(a), the following variations were tested: increasing particle diameter to 1.2 mm, increasing the spring constant ( $K_n$ ) by increasing  $E$  to  $2 \times 10^9$  Pa, decreasing  $K_n$  by decreasing  $E$  to  $5 \times 10^8$  Pa, setting the tangential spring constant ( $K_t$ ) as equal to  $K_n$  and finally switching from a Hookean contact model to a Hertzian model. While the variations in the spring constant were achieved by changing the Young's modulus, an equivalent effect could be achieved in our implementation by varying the Poisson's ratio or the characteristic velocity. For the low spring constant simulation, some particles near the very base of the shear cell may not have met the stiffness criteria given by Eq. (A21). These particles were excluded from the analysis. For the simulation run using a Hertzian contact model, while identical properties were maintained, due to differences in how  $K_n$  is defined Eq. (5) could not be applied. To ensure the particles were still rigid  $K_n$  was set such that  $(k_n/P)^{2/3} \geq 10^4$  where  $K_n = 4E^*/3$  (see Appendix A 1 for definition of  $E^*$ ) [38].

Figure 2(b) summarizes the results of these variations through comparison of the obtained dimensionless granular fluidity and packing fraction. The resultant curves collapse onto each other, despite the different properties used. Hence the effect of each on the behavior of the system is minimal. These results indicate that the microscopic definition of granular fluidity is valid over a wide range of conditions.

In addition to the factors examined in Fig. 2(b), a few further properties were considered that did not display the same collapse as observed previously. One of these factors was the particle friction, as described by the coefficient of friction,  $\mu_p$ . Figure 3(a) shows  $gd/\delta v$  plotted against  $\phi$  for  $\mu_p$  values ranging from 0.1 to 0.8 (with  $\mu_p$  for wall particles kept at 0.4). Overtop of these values a fitted form of Eq. (3) has been plotted. Details of this fitting are given in the Appendix A 5. As  $\mu_p$  increases the resulting curve shifts left, with the system becoming more dilute, and down, as lower values of  $gd/\delta v$  are obtained. This shift also means that the position where the system levels off shifts to the left and the slope of the decline at high  $\phi$  values becomes shallower as  $\mu_p$  increases. The figure shows that changing  $\mu_p$  has a fairly consistent effect on the relationship between  $gd/\delta v$



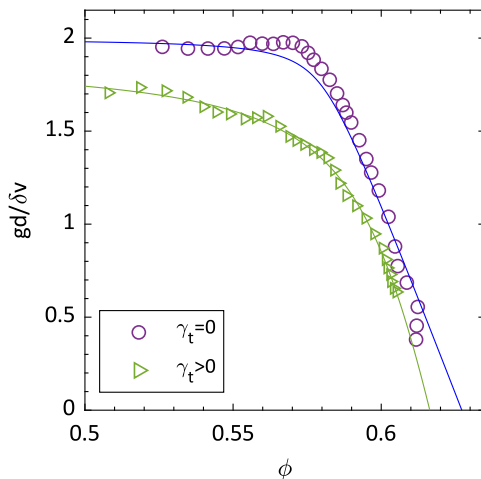


FIG. 4.  $gd/\delta v$  plotted against  $\phi$  for shear cell simulations run with ( $\gamma_t > 0$ ) and without ( $\gamma_t = 0$ ) tangential damping. The green line represents Eq. (3) fitted for the case where  $\gamma_t > 0$ .

and  $\phi$ , but as shown by the plotted lines, the underlying functional form is consistent with Eq. (3), at least over the ranges evaluated here.

As well as looking at the particle friction coefficient, friction was also examined through introducing rolling resistance into the DEM simulations. Rolling resistance was implemented using a constant directional torque (CDT) model with rolling friction ( $\mu_r$ ) set to 0.05. Figure 3(b) shows the result of introducing rolling resistance with various different values of  $\mu_p$ . The figure shows that introducing rolling resistance produces a clear shift in the curves to the left, with lower packing fractions corresponding to similar  $gd/\delta v$  values. In DEM both the coefficient of friction and rolling resistance manifest themselves in the tangential component of the force, with  $\mu_s$  acting as a limiting value, while  $\mu_r$  represents an additional torque contribution.

Another factor that affects the tangential forces is the presence of tangential damping, which accounts for the dissipation of energy by the tangential components of particle contacts. In prior simulations, tangential damping was neglected by setting the tangential damping coefficient ( $\gamma_t$ ) to 0. Figure 4 shows the effect of including tangential damping. Here tangential damping was implemented based on the spring constant and coefficient of restitution using a typical formula for  $\gamma_t$  for a Hookean contact model [26]. This figure shows that there is a substantial downward shift occurring with the introduction of tangential damping. Furthermore, insufficiently low  $\phi$  values were recovered to determine whether  $gd/\delta v$  eventually reaches a constant value, with the available data showing it continuing to rise towards 1.8–1.9.

Overall these results demonstrate that we were able to successfully duplicate the relationship recovered by Zhang and Kamrin [4] for shear cells with and without gravity. That this relationship persisted when varying a number of simulation parameters, including changing the contact model used, shows that the results are largely independent of these parameters, as would be expected if the microscopic definition for granular fluidity holds true. However, we have demonstrated that notable deviations to the relationship can occur when changing the coefficient of friction, when introducing rolling resistance and when introducing tangential damping, though these deviations do not affect the underlying functional form. As all three properties manifest themselves through the tangential forces occurring during collisions, this further suggests that it is the frictional contacts between particles that are responsible for the deviation from the expected behavior.



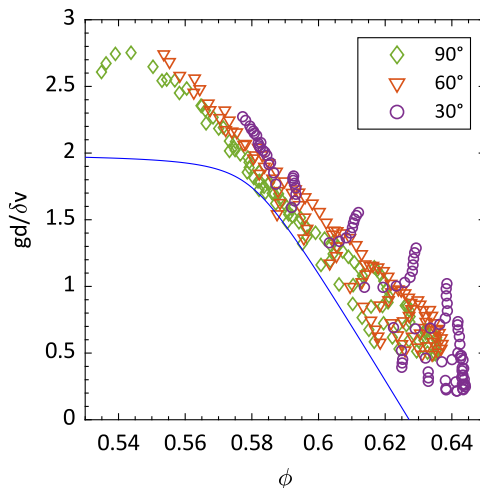


FIG. 5.  $gd/\delta v$  plotted against  $\phi$  for hoppers with different  $\theta$  values.

### B. Analysis of hopper results

Figure 5 shows the results produced for three hopper simulations where the hopper cone angle ( $\theta$ ) was set to  $90^\circ$ ,  $60^\circ$ , and  $30^\circ$ , respectively. These simulations were run with the same properties as the base shear cell simulation though, as noted, the particle diameter is slightly larger. The simulations did not include rolling resistance or tangential damping. The results show a roughly linear relationship between  $\phi$  and  $gd/\delta v$ . Further from the hopper outlet, where  $\phi$  is high, there is a great deal of scatter in the results, corresponding to the different radial positions analyzed, with lower packing fractions observed towards the walls of the hopper. Nearer to the outlet, where  $\phi$  is low, the data appear to collapse onto a line. The majority of points appear to be shifted to the right of Eq. (3), with similar  $gd/\delta v$  values associated with higher  $\phi$  values. There is some degree of variation between the different hopper geometries, particularly for the  $30^\circ$  hopper which appears to show more pronounced curvature. For the other two hoppers, any possible curvature is minimal. In all three cases, the values plotted are insufficient to determine whether  $gd/\delta v$  has leveled off. Thus it appears that changing the geometry from simple shear flow to the more complex 2D flow of the hopper geometry has affected the form of the  $gd/\delta v$  versus  $\phi$  relationship.

The analysis in Fig. 5 covers a similar range of  $\phi$  values to the shear cell analysis and is sufficient to demonstrate that variations occur when changing to a hopper geometry. However, it was desirable to see whether the levelling off of  $gd/\delta v$  at low  $\phi$  values seen in the shear cell simulations, also occurred in the hopper geometry. Therefore, an analysis of the system at low  $\phi$  was performed by coarse graining along the central axis of each hopper. Because of the limited space through the outlet, multiple radial positions were not considered. Instead, for each height a single position at a radial value of 0 (or alternatively  $x = 0$  and  $y = 0$ ) was evaluated along the central axis of the hopper. To confirm that the trends in the data with this “centerline” analysis are consistent with the earlier results, Fig. 6(a) shows a comparison between the regular analysis method, used to produce Fig. 5, and the centerline analysis for the  $60^\circ$  hopper. The figure demonstrates that the centerline analysis slightly underestimates  $gd/\delta v$  as  $\phi$  decreases. However, the overall results of both methods are in good agreement, providing confidence that the centerline analysis can be used to examine the behavior over a wide range of  $\phi$  values. Figure 6(b) shows the full centerline analysis for each hopper. Equation 3 is also plotted down to  $\phi = 0.5$  as Zhang and Kamrin [4] don’t appear to have considered  $\phi < 0.5$  when developing the equation. Figure 6(b) shows that dimensionless granular fluidity levels off at  $\phi = 0.55$ . There is a small  $\phi$  region which corresponds to the constant  $gd/\delta v$  section. For  $\phi < 0.54$  the packing fraction decreases as the outlet is approached,

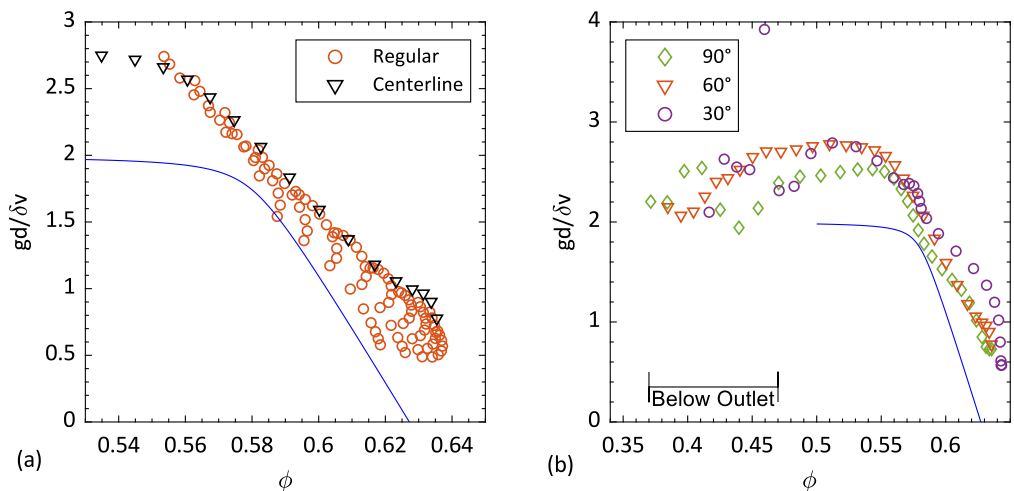


FIG. 6.  $gd/\delta v$  plotted against  $\phi$  for simulations of flow in a hopper. Panel (a) compares the centerline analysis with the regular analysis for a  $60^\circ$  hopper. Panel (b) uses the centerline analysis method to analyze hoppers with different  $\theta$  values. The heights analyzed using the centerline analysis in (b) do not correspond to the same heights used for the regular analysis.

corresponding with a slight decline in  $gd/\delta v$ . The exact position of the outlet on this figure differs for each hopper. The outlet is at around  $\phi = 0.45$  for the  $90^\circ$  hopper,  $\phi = 0.46$  for the  $60^\circ$  hopper and  $\phi = 0.49$  for the  $30^\circ$  hopper. Below the outlet the particles are in freefall and the pressure drops to approximately 0 Pa. The dimensionless granular fluidity is thus poorly resolved, leading to large fluctuations in even the time-averaged value.

Curiously, Fig. 6(b) shows that the  $30^\circ$  hopper does not level off at  $\phi = 0.58$  as Fig. 5 potentially suggests. Instead the behavior shown in Fig. 5 appears to be associated with a region approaching the outlet where the packing fraction is roughly constant. This region is seen as a small cluster of points at constant  $\phi$  and  $gd/\delta v$  on Fig. 6(b). These points follow the same trend as the other points shown for the  $30^\circ$  hopper, though their origin is unclear.

Figure 6(b) demonstrates that the hopper results have a constant  $gd/\delta v$  section, showing that their form is similar to Eq. (3). However, the constant section occurs at a higher  $gd/\delta v$  value and a lower  $\phi$  value than Eq. (3) would suggest. Further, the subsequent decline in  $gd/\delta v$  towards the outlet may indicate a flow regime transition from a dense intermediate granular flow to a dilute inertial granular flow.

Both Fig. 5 and Fig. 6 make clear that, while we do recover a form similar to Eq. (3), the hopper geometry presents clear deviations from the expected behavior. This in turn demonstrates that changing from a shear cell to a hopper affects the relationship between  $gd/\delta v$ .

#### IV. DISCUSSION

Our results demonstrate that the relationship between the dimensionless granular fluidity and the packing fraction is more complex than expected. The results in the shear cells demonstrate that the rheological behavior is independent of external properties (e.g., pressure, shear rate), consistent with previous work [4]. However, our simulations reveal a dependence on the frictional forces occurring between particles and a potential geometric effect.

The results in Fig. 3 and Fig. 4 show that the coefficient of friction, rolling resistance, and tangential damping all affect the apparent relationship between the  $gd/\delta v$  and  $\phi$ . However, they do not appear to affect the functional form of the relationship. All three of these factors influence

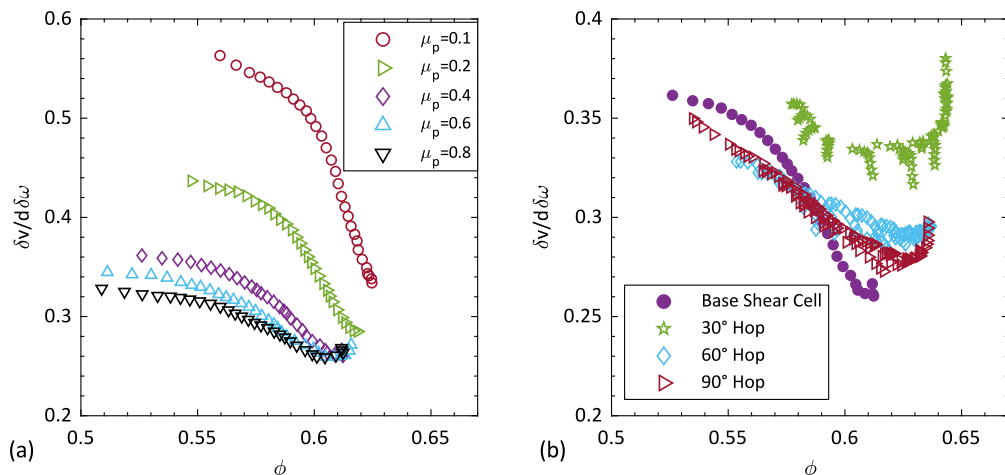


FIG. 7.  $\delta v/d\delta\omega$  plotted against  $\phi$  for, (a) shear cell simulations at different  $\mu_p$  values and (b) for hoppers with different  $\theta$  values (with the base shear cell plotted for comparison).

the tangential forces and/or torque occurring between particles, and hence are related to frictional effects in the granular flow. In their work Zhang and Kamrin [4] provided a justification for their chosen microscopic definition, i.e., Eq. (3), based on the kinetic theory of granular flow as well as an activated process model. The kinetic theory of granular flow they used did not include any dependence on  $\mu_p$  [39]. However, it has been shown that kinetic theory must incorporate a dependence on friction when extended to model dense systems [14]. The activated process model doesn't include a direct dependence on friction. However, the probability that a perturbation causes a forwards or backwards shear event is dependent on the parameters of a local  $\mu(I)$  response [40], which are in turn dependent on  $\mu_p$  [41]. The microscopic definition may also be justified directly through the  $\mu(I)$  rheology, and the related scalings between  $\phi$  and  $I$ , and  $\delta v/\dot{\gamma}d$  and  $I$  [8]. The stress response, as characterized using the  $\mu(I)$  rheology, again, has been observed to display a dependence on  $\mu_p$  [41]. Furthermore, at least in regions of dense flow, the relationship between  $\delta v/\dot{\gamma}d$  and  $I$  also shows dependence on  $\mu_p$  [42,43]. Thus, the variation observed with coefficient of friction is perhaps not surprising, indeed Zhang and Kamrin [4] themselves noted the dependence on friction, though they did not directly include it in their form of the model.

The discussed justifications also provide insight into the mechanism underlying the observed deviations. Extended kinetic theory indicates that variation with  $\mu_p$  relates to additional energy dissipation [14]. In dense, homogeneous flows this change in energy dissipation is further associated with a regime transition between frictionless, frictional sliding, and rolling collisions, as  $\mu_p$  increases [42]. The relative importance of rotational and translational motion is examined in Fig. 7(a), which plots the ratio  $\delta v/d\delta\omega$  against  $\phi$ , where  $\delta\omega$  describes the rotational velocity fluctuations (this choice in scaling is expanded upon in Appendix A7) and  $d$  the local mean diameter. Figure 7(a) demonstrates that as  $\mu_p$  increases, the rotational velocity fluctuations increase relative to the translational fluctuations (i.e., the curve shifts downwards). If the relative importance of rotational velocity fluctuations increases, it implies relatively more energy is dissipated through the rotational motion than the translational motion. The shifts in the modes of energy dissipation may in turn lead to the observed shifts in  $gd/\delta v$ .

Given that tangential damping and rolling resistance also influence the tangential forces during contacts, it is perhaps expected that they would also influence the  $gd/\delta v$  versus  $\phi$  relationship, though this has not been as clearly established. Additionally, Fig. 10 below shows that the tangential spring constant ( $K_t$ ), which affects the tangential force, does not appear to directly impact the

observed relationship. As the coefficient of friction and rolling resistance both appear to influence the  $gd/\delta v$  versus  $\phi$  relationship in a systematic manner, it should be possible to factor in their dependence into the constants in Eq. (3). Accurately incorporating tangential damping into the microscopic definition is more problematic, as it can be linked to a number of particle properties [26]. However, in general our results indicate that any microscopic definition of granular fluidity will be dependent on the parameters that characterize interparticle friction.

A comparison between the simulations of shear cells and hoppers indicates that the dimensionless granular fluidity is not solely determined by the solid fraction, even for constant friction parameters. The different behavior of these two systems suggests that geometry affects the relationship between  $gd/\delta v$  and  $\phi$ . Few other studies have investigated the microscopic definition of granular fluidity. Bhateja and Khakhar [20] touched on the definition in their work simulating 2D hopper flows. A quantitative comparison of their results with that of Zhang and Kamrin [4] was not possible, owing to the simulations being 2D. However, their results do appear to show that the relationship between  $gd/\delta v$  and  $\phi$  has a slight dependence on the outlet size. Thus, there is some prior evidence for geometry affecting the microscopic definition. The hopper is a 2D flow geometry, with properties of the flow varying radially and vertically. While Zhang and Kamrin [4] ran 3D simulations, the flows were inherently 1D (with flow properties varying along one axis only), being shear cells and chute flows. It is possible that 2D granular flows may simply behave differently to 1D granular flows. For example, 2D flows may become extensional [20], which could lead to differences in the generation and transport of granular fluidity compared to 1D flows. There is also evidence that certain complex heterogeneous flows can lead to a breakdown in fluidity as a continuous field [44], though whether this could occur in a hopper is unknown. Figure 7(b) shows the ratio of linear versus rotational velocity fluctuations in hoppers. The figure demonstrates that, in the hopper geometry, the nature of energy dissipation between the translational and rotational modes differs with what is expected based on the shear cell results, and that variation is observed with  $\theta$ . This suggests that the geometric effects may be related to, or perhaps cause, differences in energy dissipation, which could in turn result in differences in the  $gd/\delta v$  versus  $\phi$  response. However, the underlying physical cause remains unclear.

The breakdown of the relationship between  $\phi$  and  $gd/\delta v$  when certain DEM parameters are varied is not unexpected, given the empirical nature of the relationship. The fact that we could fit a form of Eq. (3) to each simulation indicates that the coefficients are particle dependent, but that otherwise the result is relatively general. The general microscopic definition can still be considered potentially valid. The evidence for geometric effects is more concerning as it shows that the microscopic definition is failing to hold even when the particle properties remain unchanged. These results suggest that other variables are affecting the relationship and so  $gd/\delta v$  is not solely a function of  $\phi$ . If  $gd/\delta v$  is a function of variables other than  $\phi$ , it means the nature of granular fluidity as a physical property and its definition as a state variable are once again uncertain.

## V. CONCLUSION

In this work we have investigated a microscopic definition for granular fluidity, that links the granular fluidity to the granular temperature and the packing fraction. We examined multiple DEM simulations of shear cell and hopper geometries. Our results for shear cells match previous work [4], confirming that the rheology of dense granular material collapses to a simple function of solid fraction for a wide variety of changes in external conditions, including the effect of gravity, confining pressure, and shear rate. However, the simulations also demonstrate that the proposed definition of granular fluidity displays dependence on the friction coefficient, on the presence of rolling resistance and on the presence of tangential damping. More importantly, it showed a complete breakdown when applied to hoppers. This breakdown demonstrates that the property of granular fluidity is not as well defined as previously thought and opens up the potential for further research into the relationship.

## ACKNOWLEDGMENTS

The author(s) wish to acknowledge the use of New Zealand eScience Infrastructure (NeSI) high performance computing facilities, consulting support and/or training services as part of this research. New Zealand's national facilities are provided by NeSI and funded jointly by NeSI's collaborator institutions and through the Ministry of Business, Innovation & Employment's Research Infrastructure programme. Supported by the Marsden Fund Council from Government funding, managed by Royal Society Te Apārangi (Grant No. MAU1712).

## APPENDIX

### 1. DEM

The Hookean model was implemented as detailed in the LIGGGHTS documentation [25,26]; the following is a brief summation of the model. For this model, collisions between spheres are modeled by having the spheres overlap in space. Subsequently, a contact force ( $\mathbf{F}$ ) is exerted on each particle, as described by the expression

$$\mathbf{F}_{\alpha\beta} = (K_n \delta \mathbf{n}_{\alpha\beta} - \gamma_n \mathbf{v}_{n,\alpha\beta}) + (K_t \delta \mathbf{t}_{\alpha\beta} - \gamma_t \mathbf{v}_{t,\alpha\beta}), \quad (\text{A1})$$

where the first bracketed term accounts for the normal force (between the two particle centers), while the second accounts for the tangential force (perpendicular to the normal force). The tangential force is truncated such that  $\mathbf{F}_t \leq \mathbf{F}_n \mu_p \cdot \delta \mathbf{n}_{\alpha\beta}$  and  $\delta \mathbf{t}_{\alpha\beta}$  are the normal and tangential overlap, respectively, while  $\mathbf{v}_{n,\alpha\beta}$  and  $\mathbf{v}_{t,\alpha\beta}$  are the relative normal and tangential particle velocities.  $\alpha$  and  $\beta$  are the two particles involved in the collision.

The normal spring constant,  $K_n$ , is described by the equation

$$K_n = \frac{16}{15} (R^*)^{0.5} E^* \left[ \frac{15 m^* u_c^2}{16 (R^*)^{0.5} E^*} \right]^{1/5}, \quad (\text{A2})$$

where  $E^*$  is defined as

$$\frac{1}{E^*} = \frac{1 - v_\alpha^2}{E_\alpha} + \frac{1 - v_\beta^2}{E_\beta}. \quad (\text{A3})$$

$R^*$  and  $m^*$  are also defined based on the colliding particles' radii ( $R$ ) and masses ( $m$ ) with  $R^{*-1} = R_\alpha^{-1} + R_\beta^{-1}$  and  $m^{*-1} = m_\alpha^{-1} + m_\beta^{-1}$ . As stated in the main part of this paper, the tangential spring constant,  $K_t$ , was typically defined as  $2K_n/7$ .

The normal damping coefficient,  $\gamma_n$  was defined as

$$\gamma_n = \sqrt{\frac{4m^* K_n}{1 + \left[ \frac{\pi}{\ln(e_r)} \right]^2}} \geq 0, \quad (\text{A4})$$

and the tangential damping coefficient,  $\gamma_t$ , when not set to 0, was defined as equal to the normal damping coefficient.

When rolling resistance was implemented, it was done so using the constant directional torque model, which introduces the additional torque contribution

$$\mathbf{T}_{rf} = \mu_r K_n R^* \delta \mathbf{n}_{\alpha\beta} \frac{\boldsymbol{\omega}_{s,\alpha\beta}}{|\boldsymbol{\omega}_{s,\alpha\beta}|}, \quad (\text{A5})$$

where  $\mu_r$  is the rolling friction coefficient and  $\boldsymbol{\omega}_{s,\alpha\beta}$  is the projection of the relative rotational velocity ( $\boldsymbol{\omega}_{\alpha\beta}$ ) onto the shear plane.

The above forces are used to solve the following expressions for each particle's motion:

$$m_\alpha \ddot{\mathbf{x}}_\alpha = \sum_\beta (\mathbf{F}_{n,\alpha\beta} + \mathbf{F}_{t,\alpha\beta}), \quad (\text{A6})$$

which describes the linear ( $xyz$ ) motion, and

$$I_{n\alpha}\dot{\boldsymbol{\omega}}_\alpha = \sum_{\beta} (\mathbf{r}_{\alpha,c} \times \mathbf{F}_{t,\alpha\beta} + \mathbf{T}_{rf,\alpha\beta}) \quad (\text{A7})$$

describes the particle's rotation. Here  $I_{n\alpha}$  is the particles inertia and  $\mathbf{r}_{\alpha,c}$  the vector running from the center of particle  $\alpha$  to the point of contact.

## 2. Definitions of key properties

The following outlines the definitions that were used for the key properties.

The equivalent shear rate  $|\dot{\gamma}|$  is defined as

$$|\dot{\gamma}| = \left( \sum_i \sum_j 2D'_{ij}D'_{ij} \right)^{0.5}, \quad (\text{A8})$$

where  $\mathbf{D}'$  denotes the deviatoric component of the deformation tensor,  $\mathbf{D}$ :

$$\mathbf{D} = \frac{1}{2}[\nabla\mathbf{u} + (\nabla\mathbf{u})^T], \quad (\text{A9})$$

where  $\mathbf{u}$  is the macroscopic velocity, and

$$D'_{ij} = D_{ij} - \frac{1}{n}\text{Tr}(\mathbf{D})\delta_{ij}, \quad (\text{A10})$$

where  $n$  is the number of dimensions,  $\delta$  is the Kronecker delta and  $\text{Tr}$  denotes the trace of a matrix.

The pressure  $P$  is defined as

$$P = -\frac{1}{n}\text{Tr}(\boldsymbol{\sigma}). \quad (\text{A11})$$

The equivalent shear stress  $|\sigma|$  is defined as

$$|\sigma| = \left( \sum_i \sum_j 0.5\sigma'_{ij}\sigma'_{ij} \right)^{0.5}, \quad (\text{A12})$$

where  $\boldsymbol{\sigma}$  is the Cauchy stress tensor and

$$\sigma'_{ij} = \sigma_{ij} + P\delta_{ij}. \quad (\text{A13})$$

The granular temperature  $T$  is defined as

$$T = \delta v^2 = \sum_i (u'_i)^2, \quad (\text{A14})$$

where  $(\mathbf{u}')^2$  is the macroscopic square velocity deviation, a measure of the typical deviation between the particle velocity and the bulk velocity. This was calculated via coarse graining using a similar equation to Eq. (7):

$$(\mathbf{u}')^2 = \frac{\sum_{\alpha} V_{\alpha} (\mathbf{u}'_{\alpha})^2 W(\mathbf{x} - \mathbf{x}_{\alpha})}{\sum_{\alpha} V_{\alpha} W(\mathbf{x} - \mathbf{x}_{\alpha})}, \quad (\text{A15})$$

where  $\mathbf{u}_{\alpha}$  has been replaced by  $(\mathbf{u}'_{\alpha})^2$ .  $\mathbf{u}'_{\alpha}$  is difference between  $\mathbf{u}_{\alpha}$  and the coarse-grained velocity at  $\mathbf{x}_{\alpha}$  only in this case obtained by interpolation of the coarse-grained instantaneous spatially averaged velocity field.

The rotational velocity and subsequently the rotational velocity fluctuations are defined in much the same way as with the linear velocity and velocity fluctuations. The coarse-grained rotational

TABLE II. List of  $P_f$ ,  $V_f$ , and  $G_f$  values used for shear cell simulations and the corresponding true values of  $V_w$ ,  $P_w$ , and  $G$  used.

$V_f = 5$	$V_w = 5 \text{ m s}^{-1}$
$V_f = 2$	$V_w = 2 \text{ m s}^{-1}$
$V_f = 1.5$	$V_w = 1.5 \text{ m s}^{-1}$
$V_f = 1$	$V_w = 1 \text{ m s}^{-1}$
$P_f = 4.9$	$P_w = 500 \text{ Pa}$
$P_f = 3$	$P_w = 300 \text{ Pa}$
$P_f = 1$	$P_w = 100 \text{ Pa}$
$G_f = 0$	$G = 0 \text{ m s}^{-1}$
$G_f = 1 (d = 0.8 \text{ mm})$	$G = 9.81 \text{ m s}^{-2}$
$G_f = 1.5 (d = 1.2 \text{ mm})$	$G = 9.81 \text{ m s}^{-2}$

velocity ( $\omega$ ) is defined as

$$\omega = \frac{\sum_{\alpha} V_{\alpha} \omega_{\alpha} W(\mathbf{x} - \mathbf{x}_{\alpha})}{\sum_{\alpha} V_{\alpha} W(\mathbf{x} - \mathbf{x}_{\alpha})}, \quad (\text{A16})$$

where  $\omega_{\alpha}$  is the particle's rotational velocity. The macroscopic square rotational velocity deviations,  $(\omega')^2$  are thus defined identically to  $(\mathbf{u}'_{\alpha})^2$ :

$$(\omega')^2 = \frac{\sum_{\alpha} V_{\alpha} (\omega'_{\alpha})^2 W(\mathbf{x} - \mathbf{x}_{\alpha})}{\sum_{\alpha} V_{\alpha} W(\mathbf{x} - \mathbf{x}_{\alpha})}, \quad (\text{A17})$$

where  $\omega'_{\alpha}$  is the difference between  $\omega_{\alpha}$  and the coarse-grained rotational velocity at  $\mathbf{x}_{\alpha}$ , obtained via interpolation of the coarse-grained instantaneous spatially averaged rotational velocity field. The value of  $\delta\omega$  is subsequently defined as

$$\delta\omega^2 = \sum_i (\omega'_i)^2. \quad (\text{A18})$$

The average diameter used in Eq. (2) was calculated using the following formula:

$$d = \frac{\sum_{\alpha} V_{\alpha} d_{\alpha} W(\mathbf{x} - \mathbf{x}_{\alpha})}{\sum_{\alpha} V_{\alpha} W(\mathbf{x} - \mathbf{x}_{\alpha})}, \quad (\text{A19})$$

where  $d_{\alpha}$  is the diameter of particle  $\alpha$ . As with the granular temperature this is effectively Eq. (7) only with the particle diameter replacing the particle velocity. This is essentially a volume weighted average diameter with the addition of the weighting from the coarse-graining function. While there are numerous other potentially valid ways to compute the average diameter [45], for the systems evaluated here the different methods should not significantly shift the obtained result.

### 3. Simulation inputs

For the purposes of replicability, Table II provides the exact values of  $G$ ,  $V_w$ , and  $P_w$  used for the shear cell simulations, along with the corresponding  $G_f$ ,  $V_f$ , and  $P_f$  values, which have been rounded both here and in the text. For the purposes of applying the dimensionless scaling,  $K_n$  should be computed with  $R^*$  equal to  $R/2$  and  $m^* = m/2$  where  $R$  and  $m$  are the particle radius and mass defined using the systems overall numerical mean diameter.

Similarly, the shear cells had the exact dimensions of 9.6 mm  $\times$  9.6 mm along the  $x$  and  $y$  dimensions, except in the case where  $d = 1.2$  mm wherein the dimensions were 14.4 mm  $\times$  14.4 mm. The hopper had an exact diameter of 24.5 mm and an outlet diameter of 9.5 mm.

The shear cell simulations were run with  $\delta t = 0.174\sqrt{m/K_n}$ , which translated to an exact time step of 1  $\mu\text{s}$ . The output files were generated every 100 000 time steps or every 0.1 s. The hopper



TABLE III. List of  $P_f$ ,  $V_f$ ,  $G_f$ , and  $\delta t$  values used for shear cell simulations where  $K_n$  or  $d$  were varied.

	$V_f$	$P_f$	$G_f$	$\delta t/(\sqrt{m/K_n})$
$E = 2 \times 10^9$ Pa	1.5	1.7	0.6	0.230
$E = 5 \times 10^8$ Pa	2.6	5.2	1.8	0.132
$d = 1.2$ mm	2	3	1.5	0.116

simulations were run with  $\delta t = 0.232\sqrt{m/K_n}$ , translating to a time step of  $2 \mu\text{s}$ . The output files were generated every 50 000 time steps, or 0.1 s.

For the case of shear cells where particle properties were varied, as shown in Fig. 2(b),  $P_w$ ,  $V_w$ ,  $G_w$ , and  $\delta t$  were set to the same values as were used for the default shear cell simulation. That is  $P_w = 300$  Pa,  $V_w = 2 \text{ m s}^{-1}$ ,  $G = 9.81 \text{ m s}^{-2}$ , and  $\delta t = 1 \mu\text{s}$ . For the case where  $K_n$  or  $d$  was varied, the corresponding dimensionless scaling parameters are given in Table III. For the case where the Hertzian model was used, owing to differences in how this model defines the spring constant, the scaling used throughout the text cannot be applied.

#### 4. Velocity fields

In order to provide an improved understanding of the nature of the systems analyzed here, Fig. 8 shows a velocity map for the default shear cell and for the  $30^\circ$  hopper taken at a snapshot in time. The colorbar shows the actual (not dimensionless) velocity, though the two values should be roughly equivalent.

#### 5. Fitting

In order to fit the microscopic definition of granular fluidity to the different simulations shown in Figs. 3(a) and 3(b) and Fig. 4, the following general form of Eq. (3) was used:

$$F(\phi) = A - \frac{(\phi - B) + \sqrt{(\phi - B)^2 + C}}{D}, \quad (\text{A20})$$

where the fitted parameters were  $A$ ,  $B$ ,  $C$  and  $D$ . The fitting was done in Matlab using the “lsqnonlin” function. Table IV summarizes the fitted constants obtained. A fitting for the case where  $\mu_p = 0.4$  is included (the base case), though this was not plotted on Fig. 3. A general trend can be observed across the different simulations, with  $A$  and  $B$  decreasing with increasing  $\mu_p$  and  $D$  increasing. Introducing rolling resistance produces a similar affect, as well as reducing  $C$ , though the general

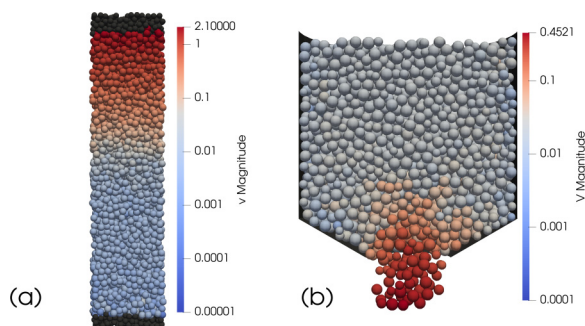


FIG. 8. Plot of particle velocity magnitude (in  $\text{m s}^{-1}$ ) at an instant in time for (a) the default shear cell, plotting the  $x$  velocity, and (b) the  $30^\circ$  hopper, plotting the  $z$  velocity. Walls/wall particles are shown in black. The full hopper is not shown, and the two figures are not to scale with one another.

TABLE IV. Values for the constants  $A$ ,  $B$ ,  $C$ , and  $D$  from fitting Eq. (A20) to different shear cell simulations.

	$A$	$B$	$C$	$D$
$\mu_p = 0.1$	2.58	0.625	$1.36 \times 10^{-4}$	0.00719
$\mu_p = 0.1$ with $\mu_r$	2.43	0.608	$1.32 \times 10^{-4}$	0.0196
$\mu_p = 0.2$	2.39	0.599	$2.03 \times 10^{-4}$	0.0293
$\mu_p = 0.4$	2.00	0.584	$0.845 \times 10^{-4}$	0.0377
$\mu_p = 0.4$ with $\mu_r$	1.94	0.568	$0.319 \times 10^{-4}$	0.0565
$\mu_p = 0.6$	1.96	0.578	$3.30 \times 10^{-4}$	0.0449
$\mu_p = 0.8$	1.83	0.570	$1.53 \times 10^{-4}$	0.0537
$\mu_p = 0.8$ with $\mu_r$	1.75	0.554	$0.319 \times 10^{-4}$	0.0732
$\gamma_t \neq 0$	1.90	0.605	$7.27 \times 10^{-4}$	0.0215

trend with  $C$  is not clear. Fitting while keeping  $C$  constant, produced only slightly worse curves while the trends in the other properties remained consistent, suggesting  $C$  is handling some of the variation occurring due to the noise in the data set.

### 6. Shear cell validity, stationarity, and basal cutoff

As part of validating the results obtained, two simulations were examined. These were the shear cell run with ( $G_f = 1$ ) and without ( $G_f = 0$ ) gravity, at the default wall velocity and pressure, so  $P_f = 3$  and with the wall velocity set with  $V_f = 2$ . For a shear cell simulation with gravity, the  $xz$  stress ( $\sigma_{xz}$ ) should be constant over the height of the shear cell, while the negative of the  $zz$  stress ( $-\sigma_{zz}$ ) should follow a roughly linear trend dropping in value to be equal to the applied pressure at the position of the wall. For a system without gravity both  $\sigma_{xz}$  and  $-\sigma_{zz}$  should be constant, with  $-\sigma_{zz}$  equaling the applied pressure [4].

Figures 9(a) and 9(b) show  $\sigma_{xz}$  and  $-\sigma_{zz}$  for the shear cell with and without gravity. Two cases are presented, one averaged over 100 time steps, as was typically done, and one averaged over 1000 time steps. The second case was used to determine the effect of number of time steps averaged

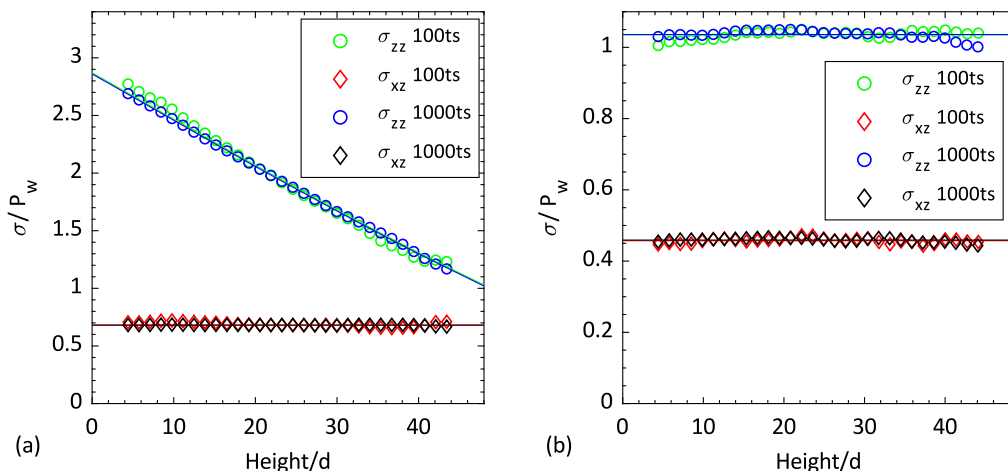


FIG. 9. Examination of a shear cell with and without gravity averaging values over 100 and 1000 time steps ( $ts$ ), respectively. Panel (a) shows  $\sigma_{xz}$  and  $-\sigma_{zz}$  for the case with gravity, (b) shows  $\sigma_{xz}$  and  $-\sigma_{zz}$  for the case without gravity. For (a) and (b) the stresses are normalized by the set wall pressure. Height is normalized by the overall system diameter (not the local mean).

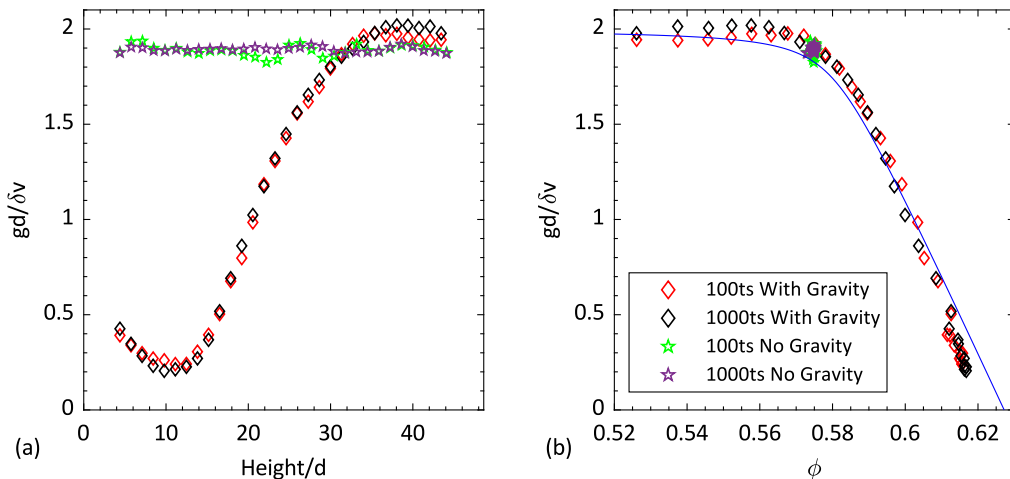


FIG. 10. Examination of a shear cell with and without gravity averaging values over 100 and 1000 time steps ( $ts$ ) respectively. Panel (a) shows  $gd/\delta v$  plotted against height, and (b) shows  $gd/\delta v$  plotted against  $\phi$ . The symbols in (a) are the same as shown in the legend for (b).

on reducing the temporal “noise” due to the inherent fluctuations present at steady state. While the sampling time could also factor into this, we found increasing it had a minimal affect on the apparent noise, suggesting sufficient strain occurred between each sampling to render each result independent. To help make the results clearer, for the stresses that should be uniform the mean value has been plotted from the base up to the average height of the top wall. For  $-\sigma_{zz}$  in the shear cell with gravity, the stress in this case should be described by

$$\frac{(\partial\sigma_{zz})}{\partial z} = -\rho\phi G. \quad (\text{A21})$$

To produce the curves shown in Fig. 9, Eq. (A21) was numerically integrated over the range of heights evaluated and shifted upwards by the constant that produced the minimum least squares error. The solid fraction could not be obtained close to the walls as coarse graining in the vicinity of the walls is not well defined. As such, linear extrapolation was used to extend the obtained integral to the system boundaries, though these boundary values are obviously only approximations.

Figure 9(a) shows that, in the case with gravity,  $-\sigma_{zz}$  over 100 time steps appears to have a slightly steeper angle compared with the integral while  $\sigma_{xz}$  appears to curve above the mean near the base and curve below near the top of the shear cell. When averaging over 1000 time steps, the expected stress responses are more clearly recovered. For Fig. 9(b) there are no apparent trends or major deviations when averaging over 100 time steps or 1000 time steps. The mean value of  $\sigma_{zz}$  is slightly high, but is within 4% of the desired value and so the difference was deemed negligible.

Figure 9 thus shows that, provided sufficient time steps are considered, the expected trends for the stresses are recovered, effectively validating the setup.

As evaluating 1000 time steps for all simulations would have been computationally expensive, in practice only 100 time steps were considered. Figure 10(a) shows the typical profiles of the dimensionless granular fluidity across the height of the shear cell in the case with and without gravity, averaging over 100 and 1000 time steps. Figure 10(b) shows the same values plotted against the packing fraction. Figures 10(a) and 10(b) show that in the case without gravity, the results when averaging over 100 time steps and 1000 time steps are functionally identical. In the case with gravity,  $gd/\delta v$  is slightly higher near the top of the shear cell, when averaging 1000 time steps rather than 100, however, the deviation here is minimal. As such it was determined that averaging over 1000

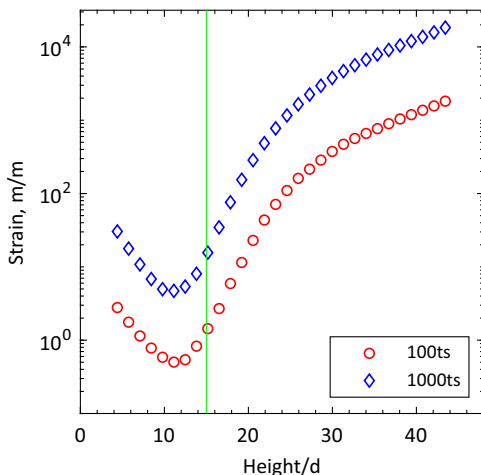


FIG. 11. Strain in a shear cell with gravity over 100 and 1000 time steps. The green line shows the chosen cutoff at a height of  $15d$ .

time steps was unnecessary and using 100 time steps would be sufficient to capture the behavior of the systems.

Figure 11 shows the strain obtained for the simulation with gravity. The strain was calculated by numerically integrating the instantaneous  $xz$  shear rate over time. The figure shows that the basal regions correspond to regions of minimal strain (strain  $\ll 1$ ). Particles in this region would not displace far from their initial position as the local velocity was low and hence the particles were nearly static. This lack of motion leads to an increased error in the calculations as both granular temperature and equivalent shear rate approaches zero. This error can be seen in Fig. 10, which includes values obtained throughout the shear cell, including in the dense region near the base of the shear cell. This error is, to an extent, mitigated by running longer simulations and considering more time steps. However, the region of interest was not this dense region, but instead the faster flowing regions where the system is at lower packing fractions and the key features of Eq. (3) are observed. As such, the nearly static dense region was removed by imposing a cutoff where the minimum height evaluated was taken as  $15d$  above the base. The exact choice of where to place this cutoff is somewhat arbitrary. It was increased to  $20d$  in one case where the system was less agitated and lowered to  $10d$  for a few cases where the systems were more agitated. In all cases the aim was simply to resolve a sufficient region of the curve while avoiding any large errors. The cutoff was only imposed for simulations with gravity as those run without gravity did not show a large region of nearly static particles.

### 7. Rotational granular fluidity

In Fig. 7 the ratio  $\delta v/d\delta\omega$  has been plotted against the packing fraction  $\phi$  in order to evaluate the relevance of differences in energy dissipation on the response of the system. The choice to represent these quantities in this way arises naturally out of the definition for dimensionless granular fluidity. We can define an rotational granular temperature as in Ref. [46]:

$$\Theta = \frac{I_n \delta\omega^2}{m}, \quad (\text{A22})$$

where  $I_n$  is the moment of inertia ( $2md^2/20$  for solid spheres). Thus the expression collapses to

$$\Theta = \frac{1}{10} d^2 \delta\omega^2. \quad (\text{A23})$$

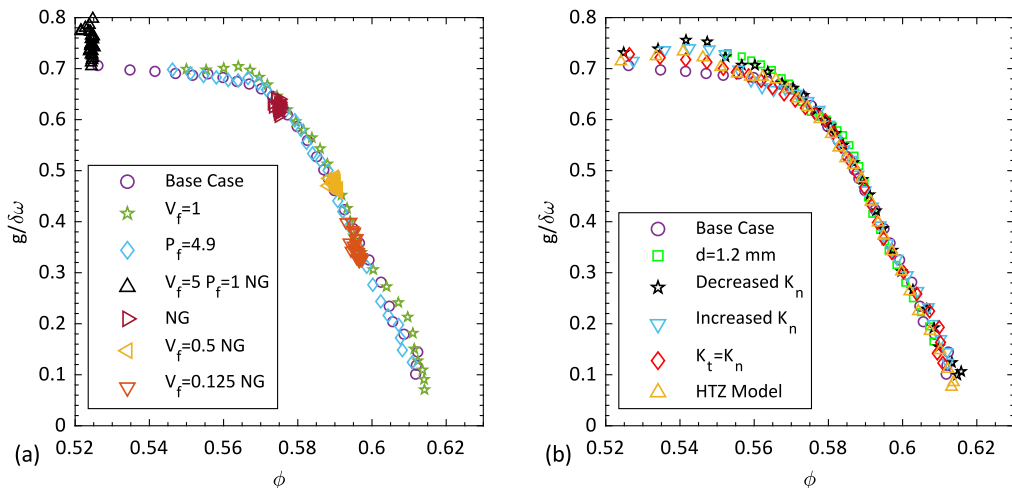


FIG. 12.  $g/\omega$  plotted against  $\phi$  for different shear cell simulations where (a)  $V_w$ ,  $P_w$ , and  $G$  are varied from the base conditions ( $V_f = 2$ ,  $P_f = 300$ ,  $G_f = 1$ ) and (b) where  $V_w$ ,  $P_w$ , and  $G$  are kept constant (as defined for the base shear cell) and different particle properties are varied.

The dimensionless granular fluidity can be redefined, replacing the square root of the linear granular temperature with the square root of the rotational granular temperature:

$$\frac{gd}{\sqrt{\frac{1}{10}d^2\delta\omega^2}} = \frac{g}{\sqrt{\frac{1}{10}\delta\omega}}. \quad (\text{A24})$$

Thus, ignoring the constant terms, we define the rotational form of the dimensionless granular fluidity as  $g/\delta\omega$ . This value has been plotted against  $\phi$  in Fig. 12 for the same simulations previously shown in Fig. 2. Figure 2 shows that, in the same way that the linear dimensionless granular fluidity

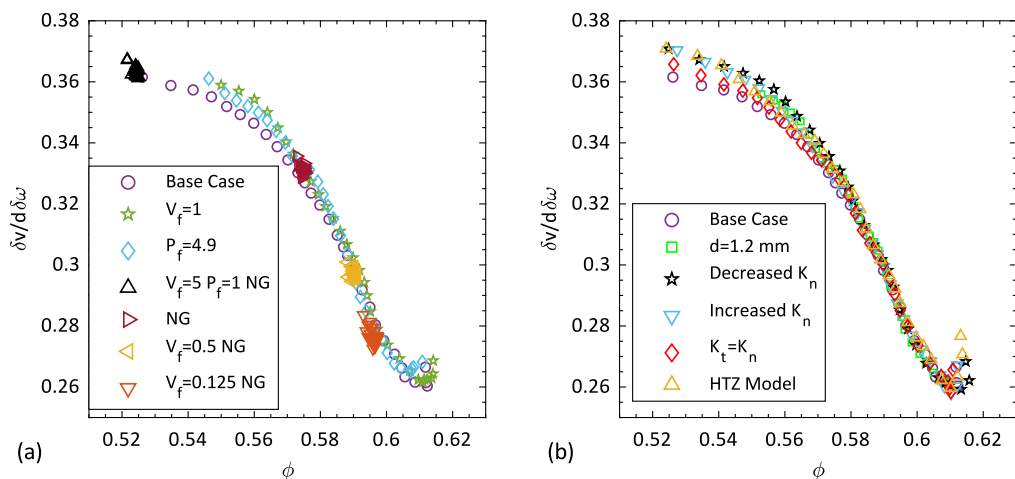


FIG. 13.  $\delta v/d\delta\omega$  plotted against  $\phi$  for different shear cell simulations where (a)  $V_w$ ,  $P_w$ , and  $G$  are varied from the base conditions ( $V_f = 2$ ,  $P_f = 3$ ,  $G_f = 1$ ) and (b) where  $V_w$ ,  $P_w$ , and  $G$  are kept constant (as defined for the base shear cell) and different particle properties are varied.

collapses onto a single function of  $\phi$ , at least for these simulations, the rotational dimensionless granular fluidity displays a similar collapse. This suggests that, we can define  $F_\omega(\phi)$  to describe the expected collapse of the rotational dimensionless granular fluidity against  $\phi$  (though we have not explored the form of this expression here).

The scaling used in Fig. 7 is derived by taking the ratio of the linear and rotational dimensionless granular fluidity:

$$\frac{g/\delta\omega}{gd/\delta v} = \frac{\delta v}{d\delta\omega} = \frac{F_\omega(\phi)}{F(\phi)} = F_R(\phi), \quad (\text{A25})$$

where  $F_R(\phi)$  is the function of  $\phi$  that describes the ratio  $\delta v/d\delta\omega$ . From the above, the choice to plot  $\delta v/d\delta\omega$  against  $\phi$  arises, since any deviation from the results obtained for the base shear cell are indicative of deviations in the dimensionless linear and rotational granular fluidity, while also providing a natural way of understanding how the relationship between linear and rotational velocity fluctuations is connected to the differing responses observed. Figure 13 shows the expected collapse for different shear cell simulations.

- 
- [1] M. Bouzid, A. Izzet, M. Trulsson, E. Clément, P. Claudin, and B. Andreotti, Non-local rheology in dense granular flows, *Eur. Phys. J. E* **38**, 125 (2015).
  - [2] K. Kamrin and G. Koval, Nonlocal Constitutive Relation for Steady Granular Flow, *Phys. Rev. Lett.* **108**, 178301 (2012).
  - [3] D. L. Henann and K. Kamrin, A predictive, size-dependent continuum model for dense granular flows, *Proc. Nat. Acad. Sci. USA* **110**, 6730 (2013).
  - [4] Q. Zhang and K. Kamrin, A Microscopic Description of the Granular Fluidity Field in Nonlocal Flow Modeling, *Phys. Rev. Lett.* **118**, 058001 (2017).
  - [5] P. Jop, Y. Forterre, and O. Pouliquen, Crucial role of sidewalls in granular surface flows: Consequences for the rheology, *J. Fluid Mech.* **541**, 167 (2005).
  - [6] P. Jop, Y. Forterre, and O. Pouliquen, A constitutive law for dense granular flows, *Nature (London)* **441**, 727 (2006).
  - [7] P. Y. Lagr e, L. Staron, and S. Popinet, The granular column collapse as a continuum: Validity of a two-dimensional Navier-Stokes model with a  $\mu(I)$ -rheology, *J. Fluid Mech.* **686**, 378 (2011).
  - [8] F. da Cruz, S. Emam, M. Prochnow, J.-N. Roux, and F. Chevoir, Rheophysics of dense granular materials: Discrete simulation of plane shear flows, *Phys. Rev. E* **72**, 021309 (2005).
  - [9] T. S. Komatsu, S. Inagaki, N. Nakagawa, and S. Nasuno, Creep Motion in a Granular Pile Exhibiting Steady Surface Flow, *Phys. Rev. Lett.* **86**, 1757 (2001).
  - [10] V. B. Nguyen, T. Darnige, A. Bruand, and E. Clement, Creep and Fluidity of a Real Granular Packing Near Jamming, *Phys. Rev. Lett.* **107**, 138303 (2011).
  - [11] GDR MiDi, On dense granular flows, *Eur. Phys. J. E* **14**, 341 (2004).
  - [12] F. Malloggi, B. Andreotti, and E. Cl ement, Nonlocal effects in sand flows on an inclined plane, *Phys. Rev. E* **91**, 052202 (2015).
  - [13] C. S. Campbell, Rapid granular flows, *Annu. Rev. Fluid Mech.* **22**, 57 (1990).
  - [14] S. Chialvo and S. Sundaresan, A modified kinetic theory for frictional granular flows in dense and dilute regimes, *Phys. Fluids* **25**, 070603 (2013).
  - [15] Z. Tang, T. A. Brzinski, M. Shearer, and K. E. Daniels, Nonlocal rheology of dense granular flow in annular shear experiments, *Soft Matter* **14**, 3040 (2018).
  - [16] K. Kamrin and D. L. Henann, Nonlocal modeling of granular flows down inclines, *Soft Matter* **11**, 179 (2015).
  - [17] D. Liu and D. L. Henann, Non-local continuum modeling of steady, dense granular heap flows, *J. Fluid Mech.* **831**, 212 (2017).

- 
- [18] T. Pähitz, O. Durán, D. N. de Klerk, I. Govender, and M. Trulsson, Local Rheology Relation with Variable Yield Stress Ratio Across Dry, Wet, Dense, and Dilute Granular Flows, *Phys. Rev. Lett.* **123**, 048001 (2019).
- [19] D. Berzi and J. T. Jenkins, Fluidity, anisotropy, and velocity correlations in frictionless, collisional grain flows, *Phys. Rev. Fluids* **3**, 094303 (2018).
- [20] A. Bhateja and D. V. Khakhar, Rheology of dense granular flows in two dimensions: Comparison of fully two-dimensional flows to unidirectional shear flow, *Phys. Rev. Fluids* **3**, 062301(R) (2018).
- [21] I. S. Aranson and L. S. Tsimring, Continuum theory of partially fluidized granular flows, *Phys. Rev. E* **65**, 061303 (2002).
- [22] P. G. Rognon, T. Miller, B. Metzger, and I. Einav, Long-range wall perturbations in dense granular flows, *J. Fluid Mech.* **764**, 171 (2014).
- [23] K. Kamrin, Non-locality in granular flow: Phenomenology and modeling approaches, *Front. Phys.* **7**, 116 (2019).
- [24] A. L. Thomas, Z. Tang, K. E. Daniels, and N. M. Vriend, Force fluctuations at the transition from quasi-static to inertial granular flow, *Soft Matter* **15**, 8532 (2019).
- [25] C. Kloss, C. Goniva, A. Hager, S. Amberger, and S. Pirker, Models, algorithms and validation for opensource DEM and CFD-DEM, *Prog. Comput. Fluid Dyn. Int. J.* **12**, 140 (2012).
- [26] LIGGGHTS(R), Public documentation, version 3.x, <https://www.cfdem.com/media/DEM/docu/Manual.html>.
- [27] M. Bouzid, M. Trulsson, P. Claudin, E. Clément, and B. Andreotti, Nonlocal Rheology of Granular Flows Across Yield Conditions, *Phys. Rev. Lett.* **111**, 238301 (2013).
- [28] P. G. Rognon, J.-N. Roux, M. Naaïm, and F. Chevoir, Dense flows of bidisperse assemblies of disks down an inclined plane, *Phys. Fluids* **19**, 058101 (2007).
- [29] S. Luding and O. Strauß, The equation of state for almost elastic, smooth, polydisperse granular gases for arbitrary density, in *Granular Gases*, Lecture Notes in Physics Vol. 564, edited by Thorsten Poschel and Stefan Luding (Springer, Berlin, 2001), pp. 389–409.
- [30] G. Salvador-Vieira, L. Staron, S. Popinet, S. Deboeuf, and P.-Y. Lagrée, Modeling flow arrest using a non-local rheology? *EPJ Web Conf.* **140**, 03045 (2017).
- [31] E. Somfai, J.-N. Roux, J. H. Snoeijer, M. van Hecke, and W. van Saarloos, Elastic wave propagation in confined granular systems, *Phys. Rev. E* **72**, 021301 (2005).
- [32] J. Slonaker, D. C. Motley, Q. Zhang, S. Townsend, C. Senatore, K. Iagnemma, and K. Kamrin, General scaling relations for locomotion in granular media, *Phys. Rev. E* **95**, 052901 (2017).
- [33] Y. Tsuji, T. Kawaguchi, and T. Tanaka, Discrete particle simulation of two-dimensional fluidized bed, *Powder Technol.* **77**, 79 (1993).
- [34] M. Otsubo, C. O’Sullivan, and T. Shire, Empirical assessment of the critical time increment in explicit particulate discrete element method simulations, *Comput. Geotech.* **86**, 67 (2017).
- [35] I. Goldhirsch, Stress, stress asymmetry and couple stress: From discrete particles to continuous fields, *Granular Matter* **12**, 239 (2010).
- [36] D. R. Tunuguntla, A. R. Thornton, and T. Weinhart, From discrete elements to continuum fields: Extension to bidisperse systems, *Comput. Part. Mech.* **3**, 349 (2016).
- [37] T. Weinhart, C. Labra, S. Luding, and J. Y. Ooi, Influence of coarse-graining parameters on the analysis of DEM simulations of silo flow, *Powder Technol.* **293**, 138 (2016).
- [38] R. C. Hurley and J. E. Andrade, Friction in inertial granular flows: Competition between dilation and grain-scale dissipation rates, *Granular Matter* **17**, 287 (2015).



- [39] C. K. K. Lun, S. B. Savage, D. J. Jeffrey, and N. Chepurniy, Kinetic theories for granular flow: Inelastic particles in Couette flow and slightly inelastic particles in a general flowfield, *J. Fluid Mech.* **140**, 223 (2006).
- [40] O. Pouliquen and Y. Forterre, A non-local rheology for dense granular flows, *Philos. Trans. R. Soc. A* **367**, 5091 (2009).
- [41] A. Favier de Coulomb, M. Bouzid, P. Claudin, E. Clément, and B. Andreotti, Rheology of granular flows across the transition from soft to rigid particles, *Phys. Rev. Fluids* **2**, 102301(R) (2017).
- [42] E. DeGiuli, J. N. McElwaine, and M. Wyart, Phase diagram for inertial granular flows, *Phys. Rev. E* **94**, 012904 (2016).
- [43] D. B. Nagy, P. Claudin, T. Börzsönyi, and E. Somfai, Flow and rheology of frictional elongated grains, *New J. Phys.* **22**, 073008 (2020).
- [44] M. Bouzid, M. Trulsson, P. Claudin, E. Clément, and B. Andreotti, Microrheology to probe non-local effects in dense granular flows, *Europhys. Lett.* **109**, 24002 (2015).
- [45] Y. Gu, A. Ozel, and S. Sundaresan, Rheology of granular materials with size distributions across dense-flow regimes, *Powder Technol.* **295**, 322 (2016).
- [46] J. T. Jenkins and C. Zhang, Kinetic theory for identical, frictional, nearly elastic spheres, *Phys. Fluids* **14**, 1228 (2002).